The Naval Research Laboratory's Coupled Ocean/Atmosphere Mesoscale Prediction System (COAMPS)

RICHARD M. HODUR

Marine Meteorology Division, Naval Research Laboratory, Monterey, California

(Manuscript received 22 April 1996, in final form 8 October 1996)

ABSTRACT

The three-dimensional Coupled Ocean/Atmosphere Mesoscale Prediction System (COAMPS) has been developed by the Naval Research Laboratory. COAMPS consists of an atmospheric data assimilation system comprising data quality control, analysis, initialization, and nonhydrostatic forecast model components, as well as a hydrostatic ocean model. The models can be integrated simultaneously so that the surface fluxes of heat, momentum, and moisture are exchanged across the air–water interface every time step. Optionally, either the atmospheric or ocean model can be used as a stand-alone system.

The atmospheric component of COAMPS was used for operational support for the America[3] team in the 1995 America's Cup races. Results of these forecasts indicated the necessity of data assimilation to reduce model spinup in the first 6 h of the forecast. Accurate forecasts of the low-level wind in the coastal race area was accomplished by utilizing triply nested grids to attain the necessary high resolution to resolve the local wind patterns and the underlying surface terrain field. Two idealized simulations of a tropical cyclone were performed with COAMPS. In the first simulation, only the atmospheric model was used, assuming a fixed sea surface temperature (SST). A realistic structure developed with spiral bands of convection present outside the inner eyewall. These spiral bands occasionally contracted inward resulting in rapid fluctuations in the intensity of the tropical cyclone. In the second simulation, the ocean model was run simultaneously with the atmospheric model. The SST cooled over 8°C over a small area within the radius of maximum winds, resulting in a much weaker system. However, there appeared to be little effect on the overall strength of the system, as measured by the tangential velocities outside the radius of maximum winds.

1. Introduction

Improved understanding of physical processes, dramatic improvements in computer technology, increased observational networks, and the availability of detailed surface parameters such as terrain height and soil type have made possible the numerical prediction of some meso-β-scale atmospheric phenomena. Predictions on these scales imply that the hydrostatic approximation may be invalid at times, particularly for convection and smaller-scale topographic features where the vertical wavelength is a significant fraction of the horizontal wavelength and therefore the vertical acceleration term cannot be ignored. The concept of using the nonhydrostatic form of the equations as a prediction tool started with the work of Ogura and Charney (1962) and Ogura and Phillips (1962). However, it was not until the 1970s that numerical models based on the nonhydrostatic equations were developed. Several of these models were used to study convective processes (Miller and Pearce 1974; Schlesinger 1975; Klemp and Wilhelmson 1978; Clark 1979; Tripoli and Cotton 1982), while others studied mountain flows (Clark 1977; Durran and Klemp 1983; Schumann 1987; Xue and Thorpe 1991). U.K. Meteorological Office has developed a nonhydrostatic model for operational use (Tapp and White 1976; Carpenter 1979), and more recently Dudhia (1993) and Tripoli (1992a) have developed nonhydrostatic models.

One of the problems in dealing with the nonhydrostatic equations is that they allow for rapidly propagating sound waves, thereby limiting the time step of the model. The anelastic approximation (Ogura and Phillips 1962) eliminates the sound waves but necessitates the solution of a three-dimensional elliptic equation every time step for pressure or geopotential, which can be computationally expensive (Miller and Pierce 1974; Clark 1977; Xue and Thorpe 1991). This can also be true for systems that do not use the anelastic approximation (Tapp and White 1976). Klemp and Wilhelmson (1978) used the fully compressible equations with a time-splitting method, which allowed for large time steps to be taken for the slow modes and shorter time steps for the faster sound modes. This time-splitting technique, coupled with semi-implicit differencing in the vertical, made the computational expense of the integration of the compressible form of the

Corresponding author address: Dr. Richard M. Hodur, Marine Meteorology Division, Naval Research Laboratory, 7 Grace Hopper Avenue, Monterey, CA 93943-5502.
E-mail: hodur@nrlmry.navy.mil

nonhydrostatic equations competitive with the anelastic form. The quasi-compressible approximation (Chorin 1967), which artificially slows down the sound waves, is an alternative method to allow for larger time steps in the fully compressible equations (Droegemeier and Wilhelmson 1987).

Use of nonhydrostatic models such as those described above are necessary for the prediction of atmospheric scales of motion at and below meso-β. These phenomena can be created in two ways, either through external or internal forcing. The externally forced modes can result from the interaction of the flow with sharp terrain, irregularly shaped coastlines, and/or sharp gradients in parameters such as the surface roughness, surface albedo, ground temperature, soil moisture, and sea surface temperature. Internally forced modes can result from instabilities characteristic of some flows or through scale interactions within the flow. The prediction of the externally forced modes depends critically on the correct specification of the lower boundary. Over land, this implies the use of high-resolution fields for parameters such as the terrain height, surface roughness, albedo, and soil and vegetation type and the utilization of a soil model for the prediction of the ground temperature and wetness. Over water, this implies the use of a detailed description of the sea surface temperature, and in cases where there exists strong interactions between the atmosphere and ocean, such as the tropical cyclone, an ocean model should be coupled to the atmospheric model to incorporate the changes to the ocean temperature and currents as they occur. The prediction of the internally forced modes depends critically on the initial three-dimensional representation of the atmosphere, possibly at or below the resolution of the feature one is trying to simulate. This may require observational networks that have a much higher spatial and temporal resolution than are routinely used today.

The Naval Research Laboratory (NRL) has developed a system that is capable of predicting mesoscale atmospheric phenomena down to the meso-β scale that are externally forced through interactions with the lower boundary. Future versions of this system will address the prediction of internally forced mesoscale phenomena. This system is referred to as the Coupled Ocean/Atmosphere Mesoscale Prediction System (COAMPS) and includes an atmospheric data assimilation system comprised of data quality control, analysis, initialization, and nonhydrostatic atmospheric model components, as well as a hydrostatic ocean model. The two models can be used separately or in a fully coupled mode. The purpose of this paper is to describe the current structure of COAMPS and to show results from experiments to demonstrate the utility of this prediction system for operational forecasting of forced mesoscale phenomena and to illustrate COAMPS ability to realistically simulate internally forced mesoscale phenomena in idealized experiments. The atmospheric data assimilation system and the ocean model are described in section 2. One operational application for the 1995 America's Cup races and two simulations of an idealized tropical cyclone are described in section 3. A summary and conclusions are given in section 4.

2. COAMPS description

The COAMPS atmospheric model is designed to be used for idealized and real-data simulations. Idealized initial conditions are typically set up through a user-supplied subroutine that specifies all initial fields through analytic functions and/or empirical data. For real-data simulations, COAMPS uses a complete mesoscale atmospheric data assimilation system, comprised of data quality control, analysis, initialization, and forecast model components. Currently the COAMPS ocean model can only perform idealized experiments and contains no provisions for data assimilation. The following sections describe the major components that make up COAMPS.

a. Grid configuration

The Arakawa C grid is used by both the atmospheric and ocean models. For real data, the polar stereographic, Lambert conformal, Mercator, or spherical grid projections are allowed. The model grid projection is specified along with the latitude and longitude of any one point in the grid, making COAMPS globally relocatable and applicable for forecasting in the polar, midlatitude, and equatorial regions. For idealized experiments, a Cartesian grid is used. Currently only the COAMPS atmospheric model can utilize nested grids. Any number of meshes are allowed with a ratio of 3:1 reduction in grid spacing between the grids. The inner grids can be specified arbitrarily within the confines of the next coarser grid, but at present, the grids are not allowed to move during the forecast. Typically, the grids utilize one-way interaction, although an option exists for two-way interaction. The atmospheric model utilizes the sigma-z vertical coordinate (Gal-Chen and Somerville 1975). The ocean model uses the z-coordinate system and currently does not incorporate terrain.

b. Initial fields

Several fields describing the surface conditions must be set. The surface terrain height is obtained from either the U.S. Navy 20′ resolution terrain field or the Defense Mapping Agency (DMA) Digital Terrain Elevation Data (DTED) level 1 data (100-m resolution). Either database can be bilinearly interpolated to the model grid. In addition to the terrain height, the surface albedo, surface roughness, ground wetness, and ground temperature must be specified initially. Monthly climatological global fields of albedo and surface roughness are bilinearly interpolated to the COAMPS grid(s). Over water, the albedo is set to 0.09. If available, the ground wetness

and ground temperature from the previous COAMPS forecast is used. In the event that these fields are not available, monthly climatological global fields of ground wetness are bilinearly interpolated to the COAMPS grid(s) over land points, the ground wetness is set to 1.0 over water points, and the initial ground temperature is set to the lowest model temperature over land points. The sea surface temperature (SST) is set by bilinearly interpolating the Fleet Numerical Meteorology and Oceanography Center (FNMOC) global SST analysis to the COAMPS grid(s).

The quality control (QC) algorithms for atmospheric observational data used in COAMPS are described by Baker (1992). These algorithms are used to screen the data for their integrity and representativeness. Some of the tasks that the QC program performs are eliminate redundant observations, check the observations against climatological limits, check vertical soundings for hydrostatic consistency, check the vertical wind shear in terms of both the speed and direction, check radiosondes against the first guess and neighboring observations, and check the position of ships relative to their position given in previous reports.

A multivariate optimum interpolation (MVOI) analysis technique (Lorenc 1986) is used to map the observations to the model grid(s). The MVOI uses the volume method to construct separate analyses for each nested grid, with the volume size on each grid predefined based on the density of observations. The analysis is performed on 16 pressure levels from 1000 to 10 mb. The wind observations are obtained from radiosondes, pibals, AIREPS, ACARS, SSM/I, surface, and cloud track winds. Heights and thicknesses are obtained from radiosondes, DMSP, and NOAA satellites. The analysis can be used to perform either a full or incremental update. In the full update cycle, the analyzed fields are interpolated from the analysis levels to the model vertical levels. In the incremental update cycle, the analysis increments to the first guess are interpolated in the vertical to the model vertical levels and added to the most recent model forecast on the model vertical levels.

Once the initial fields are interpolated to the model levels, they must be initialized to reduce the generation of spurious high-frequency oscillations. Currently the only balance that is imposed is that the vertical perturbation pressure gradient must be in hydrostatic balance with the buoyancy term in the vertical equation of motion. This is accomplished through a variational method similar to that described in Barker (1980) and assures that no vertically propagating sound waves will be generated at the start of the forecast.

c. Atmospheric model

The COAMPS atmospheric model is comprised of the nonhydrostatic, compressible form of the dynamics (Klemp and Wilhelmson 1978) and parameterizations for subgrid-scale mixing (Deardorff 1980), surface fluxes (Louis et al. 1982), explicit moist physics (Rutledge and Hobbs 1983), cumulus convective processes (Kain and Fritsch 1990, 1993), and radiation (Harshvardan et al. 1987). The vertical coordinate σ is chosen to allow for flow over an irregular surface (Gal-Chen and Somerville 1975), where

$$\sigma = z_{\text{top}}\left(\frac{z - z_{\text{sfc}}}{z_{\text{top}} - z_{\text{sfc}}}\right), \tag{1}$$

where z_{top} is the depth of the model domain and z_{sfc} is the terrain height. The complete set of the prognostic equations is as follows:

$$\frac{\partial u}{\partial t} + C_p\theta_v\left(\frac{\partial \pi'}{\partial x} + G_x\frac{\partial \pi'}{\partial \sigma}\right) + K_D\left(\frac{\partial D_3}{\partial x} + G_x\frac{\partial D_3}{\partial \sigma}\right) = -u\frac{\partial u}{\partial x} - v\frac{\partial u}{\partial y} - \dot{\sigma}\frac{\partial u}{\partial \sigma} + fv + D_u + K_H\nabla^4 u \tag{2}$$

$$\frac{\partial v}{\partial t} + C_p\theta_v\left(\frac{\partial \pi'}{\partial y} + G_y\frac{\partial \pi'}{\partial \sigma}\right) + K_D\left(\frac{\partial D_3}{\partial y} + G_y\frac{\partial D_3}{\partial \sigma}\right) = -u\frac{\partial v}{\partial x} - v\frac{\partial v}{\partial y} - \dot{\sigma}\frac{\partial v}{\partial \sigma} - fu + D_v + K_H\nabla^4 v \tag{3}$$

$$\frac{\partial w}{\partial t} + C_p\theta_v G_z\frac{\partial \pi'}{\partial \sigma} + K_D G_z\frac{\partial D_3}{\partial \sigma} = g\left(\frac{\theta'}{\bar{\theta}} + 0.608q_v' - q_c - q_r - q_i - q_s\right) - u\frac{\partial w}{\partial x} - v\frac{\partial w}{\partial y} - \dot{\sigma}\frac{\partial w}{\partial \sigma} + D_w + K_H\nabla^4 w \tag{4}$$

$$\frac{\partial \pi'}{\partial t} + \frac{\bar{c}^2}{C_p\bar{\rho}\bar{\theta}_v^2}(D_3) = -u\frac{\partial \pi'}{\partial x} - v\frac{\partial \pi'}{\partial y} - \dot{\sigma}\frac{\partial \pi'}{\partial \sigma} - \frac{R_d\bar{\pi}}{c_v}\nabla_3\cdot\mathbf{V} + \frac{c^2}{C_p\theta_v^2}\frac{d\theta_v}{dt} \tag{5}$$

$$\frac{\partial \theta}{\partial t} = -u\frac{\partial \theta}{\partial x} - v\frac{\partial \theta}{\partial y} - \dot{\sigma}\frac{\partial \theta}{\partial \sigma} + \frac{Q_\theta}{\bar{\rho}} + D_\theta + K_H\nabla^4(\theta - \theta_{\text{std}}) \tag{6}$$

$$\frac{\partial e}{\partial t} = -u\frac{\partial e}{\partial x} - v\frac{\partial e}{\partial y} - \dot{\sigma}\frac{\partial e}{\partial \sigma} + \text{BP} + \text{SP} + D_e + K_B\nabla^4 e - \epsilon \tag{7}$$

$$\frac{\partial q_v}{\partial t} = -u\frac{\partial q_v}{\partial x} - v\frac{\partial q_v}{\partial y} - \dot{\sigma}\frac{\partial q_v}{\partial \sigma} + D_{q_v} + K_H\nabla^4(q_v - q_v^*) + \frac{S_v}{\rho} \tag{8}$$

$$\frac{\partial q_c}{\partial t} = -u\frac{\partial q_c}{\partial x} - v\frac{\partial q_c}{\partial y} - \dot{\sigma}\frac{\partial q_c}{\partial \sigma} + D_{q_c} + K_H\nabla^4 q_c + \frac{S_c}{\rho} \tag{9}$$

$$\frac{\partial q_r}{\partial t} = -u\frac{\partial q_r}{\partial x} - v\frac{\partial q_r}{\partial y} - \dot{\sigma}\frac{\partial q_r}{\partial \sigma} + \frac{G_z}{\overline{\rho}}\frac{\partial}{\partial \sigma}(\overline{\rho}V_r q_r) + D_{q_r} + K_H\nabla^4 q_r + \frac{S_r}{\rho} \quad (10)$$

$$\frac{\partial q_i}{\partial t} = -u\frac{\partial q_i}{\partial x} - v\frac{\partial q_i}{\partial y} - \dot{\sigma}\frac{\partial q_i}{\partial \sigma} + D_{q_i} + K_H\nabla^4 q_i + \frac{S_i}{\rho} \quad (11)$$

$$\frac{\partial q_s}{\partial t} = -u\frac{\partial q_s}{\partial x} - v\frac{\partial q_s}{\partial y} - \dot{\sigma}\frac{\partial q_s}{\partial \sigma} + \frac{G_z}{\overline{\rho}}\frac{\partial}{\partial \sigma}(\overline{\rho}V_s q_s) + D_{q_s} + K_H\nabla^4 q_s + \frac{S_s}{\rho}. \quad (12)$$

Equations (2)–(12) are developed using the equation of state

$$p = \rho R_d T_v, \quad (13)$$

the definition of the virtual temperature

$$T_v = T(1.0 + 0.608q_v), \quad (14)$$

the Exner function

$$\pi = \left(\frac{p}{p_{00}}\right)^{R_d/C_p}, \quad (15)$$

where

$$\dot{\sigma} = G_x u + G_y v + G_z w \quad (16)$$

$$G_x = \frac{\partial \sigma}{\partial x} = \left(\frac{\sigma - z_{\text{top}}}{z_{\text{top}} - z_{\text{sfc}}}\right)\frac{\partial z_{\text{sfc}}}{\partial x} \quad (17)$$

$$G_y = \frac{\partial \sigma}{\partial y} = \left(\frac{\sigma - z_{\text{top}}}{z_{\text{top}} - z_{\text{sfc}}}\right)\frac{\partial z_{\text{sfc}}}{\partial y} \quad (18)$$

$$G_z = \frac{\partial \sigma}{\partial z} = \frac{z_{\text{top}}}{z_{\text{top}} - z_{\text{sfc}}}. \quad (19)$$

In Eqs. (2)–(15), p is the pressure; ρ the density; R_d the gas constant for dry air; T the temperature; q_v, q_c, q_r, q_i, and q_s the mixing ratios of water vapor, cloud droplets, raindrops, ice crystals, and snowflakes, respectively; p_{00} a constant reference pressure; C_p the specific heat at constant pressure for the atmosphere; u, v, and w the wind components in the x, y, and z directions, respectively; f the Coriolis force; g the acceleration due to gravity; S_v, S_c, S_r, S_i, and S_s sources and sinks of q_v, q_c, q_r, q_i, and q_s, respectively; Q_θ sources and sinks of heat; V_r and V_s the terminal velocities of raindrops and snowflakes, respectively; θ_{std} the standard atmospheric temperature; q_v^* the saturation mixing ratio corresponding to the standard atmospheric temperature; and D_3 the density and potential temperature–weighted three-dimensional divergence,

$$D_3 = \left(\frac{\partial}{\partial x} + G_x\frac{\partial}{\partial \sigma}\right)(\overline{\rho}\overline{\theta}_v u) + \left(\frac{\partial}{\partial y} + G_y\frac{\partial}{\partial \sigma}\right)(\overline{\rho}\overline{\theta}_v v) + G_z\frac{\partial(\overline{\rho}\overline{\theta}_v w)}{\partial \sigma}. \quad (20)$$

The speed of sound for the mean state, $\overline{c}$, is defined as

$$\overline{c} = \left(\frac{C_p R_d \overline{\pi}\overline{\theta}_v}{C_v}\right)^{1/2}, \quad (21)$$

where C_v is the specific heat at constant volume for the atmosphere. In Eqs. (2)–(12) and (21), the variables π and θ have been decomposed as

$$( ) = \overline{( )} + ( )', \quad (22)$$

where the overbar denotes the initial mean state, which is a function of z only, and the prime denotes deviations from this mean. The mean state follows the hydrostatic relationship

$$G_z\frac{\partial \overline{\pi}}{\partial \sigma} = -\frac{g}{C_p\overline{\theta}_v}. \quad (23)$$

The terms D_u, D_v, D_w, and D_θ represent subgrid-scale mixing and can be treated following Mellor and Yamada (1974) or, optionally, by Therry and Lacarrère (1983). In Eq. (7), BP is the buoyancy production term, SP is the shear production term, ϵ is the dissipation rate, and all the other variables are as described previously. The buoyancy production is defined as

$$\text{BP} = -\frac{G_z g K_h}{\theta}\frac{\partial \theta_v}{\partial \sigma}, \quad (24)$$

and the shear production is defined as

$$\text{SP} = K_m\left[\left(G_z\frac{\partial u}{\partial \sigma}\right)^2 + \left(G_z\frac{\partial v}{\partial \sigma}\right)^2\right]. \quad (25)$$

Separate vertical eddy mixing coefficients are used for momentum, K_{mV},

$$K_{mV} = S_m l_V e^{-1/2}, \quad (26)$$

and for the scalar variables, K_{hV},

$$K_{hV} = S_h l_V e^{-1/2}, \quad (27)$$

where l_V represents the vertical mixing length (Mellor and Yamada 1974; Therry and Lacarrère 1983).

The treatment of clouds and precipitation is handled as follows. For grid spacings greater than some specified value (currently 10 km is used), COAMPS uses the Rutledge and Hobbs (1983) explicit treatment of the moist physics for the nonconvective clouds and precipitation and the cumulus parameterization (Kain and Fritsch 1990, 1993) for the convective clouds and precipitation. For grid spacings at or below the specified value, the explicit moist physics parameterization is used for both the nonconvective and convective clouds and precipitation. Therefore, at these resolutions, COAMPS performs as a cloud model.

Over land, the ground temperature T_g and ground moisture q_{vg} are computed as

$$\frac{\partial T_g}{\partial t} = \frac{1}{C_g}(S\downarrow + L\downarrow - \sigma_{\rm SB}T_g^4 - C_pF_{\rm SH} - L_vF_{\rm LH}) - K_g(T_g - T_{gc}) \quad (28)$$

and

$$q_{vg} = W_g q_{vs} + (1 - W_g)q_{vb}, \quad (29)$$

where C_g is the heat capacity of the ground, defined as

$$C_g = 4.24 \times 10^4\{27.5\ [0.387 + 0.15W_g(1 + W_g)]\}^{1/2}, \quad (30)$$

and $S\downarrow$ is the incoming solar radiation; $L\downarrow$ is the downward longwave radiation; $\sigma_{\rm SB}$ is the Stefan–Boltzmann constant; C_p is the specific heat at constant pressure; L_v is the latent heat of vaporization; $F_{\rm SH}$ and $F_{\rm LH}$ are the surface sensible and latent heat fluxes, respectively; K_g is the relaxation constant (1.818×10^{-5} s^{-1}); T_{gc} is a climatological deep soil temperature; q_{vs} is the saturation vapor pressure associated with T_g; q_{vb} is the vapor pressure at the lowest model level; and W_g is the ground wetness, obtained using the Louis (1979) formulation

$$\frac{\partial W_g}{\partial t} = \frac{(P + F_{\rm LH})}{C_w} + \frac{(W_{gc} - W_g)}{\tau_{W_g}}, \quad (31)$$

where P is the precipitation, F_{LH} is the latent heat flux (positive downward), C_w is the moisture capacity of the ground (taken to be 0.02 m), W_{gc} is the deep soil moisture obtained from climatological tables, and τ_{W_g} is the restoring timescale (24 h) of the deep soil moisture.

The solution of continuous equations on a discrete grid inevitably leads to the generation of spurious waves due to truncation errors, boundary reflections, etc. To prevent these small sources of energy from growing and contaminating the forecasts, we have included a background fourth-order diffusion to all prognostic variables except for π'. The form of this operator, for any variable α, is $K_B\nabla^2(\nabla^2\alpha)$, which allows us to compute $\nabla^2\alpha$ first, use this on the grid rows/columns immediately adjacent to the boundaries, and then compute $\nabla^2(\nabla^2\alpha)$ for the remaining interior points. The diffusion is carried out on the σ surfaces. To prevent erroneous diffusion of the mean potential temperature and the mean mixing ratio along the sigma-surfaces, only deviations from the standard atmospheric potential temperature and from the saturated mixing ratio corresponding to the standard atmospheric temperature are diffused in Eqs. (6) and (8), respectively. The coefficient is chosen such that the ratio $(K_B\Delta x\Delta y)/\Delta t_a = 0.025$ for the second-order points and $(K_B\Delta x^2\Delta y^2)/\Delta t_a = -0.0025$ for the fourth-order points. The terms involving K_D represent divergence damping (Skamarock and Klemp 1992), where K_D is the diffusion coefficient. The K_B is a coefficient for fourth-order diffusion used to control high-frequency oscillations generated by solving the continuous equations on a discrete grid.

Several options are available for the lateral boundary conditions. For idealized simulations, either fixed, periodic, or radiation boundary conditions can be used. For the radiation conditions, all boundary values are set to their initial values at inflow points. At outflow points, the normal velocity, v_n, is computed using upstream differencing,

$$\frac{\partial v_n}{\partial t} = -(v_n + c_*)\frac{\partial v_n}{\partial n}, \quad (32)$$

where v_n represents the velocity normal to the boundary and c_* is an estimate of the fastest-moving gravity wave directed out of the domain. The value of c_* can be specified as a constant or computed following the method described by Miller and Thorpe (1981). All other variables, other than v_n, are linearly extrapolated to the boundary on outflow. For real data simulations, either Davies (1976) or Perkey–Kreitzberg (1976) boundary conditions can be used. The data for either of these are obtained from the most recent forecast from the Navy Operational Global Atmospheric Prediction System (NOGAPS; Hogan and Rosmond 1991). The NOGAPS fields are horizontally interpolated using a bicubic spline to the COAMPS coarse grid, then interpolated in the vertical to the model vertical coordinate. The time interval between fields can be set to any hourly value but depends on what time interval the NOGAPS fields are available.

d. Ocean model

The COAMPS ocean model is capable of representing the deep (barotropic) response in the ocean, as well as resolving the mixing processes within the mixed layer. The incompressible, hydrostatic equations similar to those described by Chang (1985) are used with two modifications. First, the axisymmetric form of the equations is extended to three dimensions. Second, the predictive equation for the density ρ is replaced with predictive equations for temperature T and salinity S, and the equation of state (Gill 1982) is used to diagnose the density from the temperature, salinity and pressure p. The equations become

$$\frac{\partial \bar{u}}{\partial t} = \overline{\left(-u\frac{\partial u}{\partial x} - v\frac{\partial u}{\partial y} - w\frac{\partial u}{\partial z} + fv + D_u + K_B\nabla^4 u\right)} - \frac{1}{\rho_0}\frac{\partial \bar{p}_r}{\partial x} \quad (33)$$

$$\frac{\partial u'}{\partial t} = \left(-u\frac{\partial u}{\partial x} - v\frac{\partial u}{\partial y} - w\frac{\partial u}{\partial z} + fv + D_u + K_B\nabla^4 u\right)' - \frac{1}{\rho_0}\frac{\partial p_r'}{\partial x} \quad (34)$$

$$\frac{\partial \bar{v}}{\partial t} = \overline{\left(-u\frac{\partial v}{\partial x} - v\frac{\partial v}{\partial y} - w\frac{\partial v}{\partial z} - fu + D_v + K_B\nabla^4 v\right)} - \frac{1}{\rho_0}\frac{\partial \bar{p}_r}{\partial y} \tag{35}$$

$$\frac{\partial v'}{\partial t} = \left(-u\frac{\partial v}{\partial x} - v\frac{\partial v}{\partial y} - w\frac{\partial v}{\partial z} - fu + D_v + K_B\nabla^4 v\right)' - \frac{1}{\rho_0}\frac{\partial p'_r}{\partial y} \tag{36}$$

$$\frac{\partial T}{\partial t} = -u\frac{\partial T}{\partial x} - v\frac{\partial T}{\partial y} - w\frac{\partial T}{\partial z} + D_T + K_B\nabla^4 T \tag{37}$$

$$\frac{\partial S}{\partial t} = -u\frac{\partial S}{\partial x} - v\frac{\partial S}{\partial y} - w\frac{\partial S}{\partial z} + D_S + K_B\nabla^4 S \tag{38}$$

$$\frac{\partial h}{\partial t} = -\frac{\partial (hu_s)}{\partial x} - \frac{\partial (hv_s)}{\partial y} - H\left(\frac{\partial u}{\partial x} + \frac{\partial v}{\partial y}\right) \tag{39}$$

$$\rho = f_\rho(T, S, p), \tag{40}$$

where all the variables are defined as above for the atmospheric model, except that here u, v, and w are ocean current speeds in the x, y, and z directions; the subscript s refers to the surface; D_T and D_S represent subgrid-scale mixing of the temperature and salinity, respectively; H is the undisturbed mean height of the ocean; h is the deviation height from this mean, referred to as the free surface height; f_ρ symbolically represents the equation of state; and p_r is the reference pressure, expressed as

$$p_r(z) = p(z) - g\rho_0(H - z), \tag{41}$$

where ρ_0 is the mean ocean density. The momentum equations have been decomposed into a vertical mean (barotropic mode) and the perturbation from this mean (baroclinic modes), expressed as

$$( ) = \bar{( )} + ( )'. \tag{42}$$

Therefore, the mean and perturbation reference pressures become

$$\bar{p}_r = \frac{\bar{\rho} g h}{2} + g\overline{\rho' z} + \rho_s g h \tag{43}$$

and

$$p'_r = p_r - \bar{p}_r, \tag{44}$$

respectively, where ρ_s is the surface density.

The complete set of equations for the ocean model is comprised of (33)–(40), (43), and (44). As in the atmospheric model, the equations are solved on the staggered, scheme C grid. A similar staggering is used in the vertical, with w defined at the interface between the layers and all other variables defined at the middle of each layer. All derivatives are computed to second-order accuracy except the horizontal diffusion, which uses fourth-order accurate approximations to damp only the shortest wavelengths. High-frequency time oscillations are controlled using the Robert (1966) time filter.

The subgrid-scale mixing in the COAMPS ocean model is similar to that used in the FNMOC Thermodynamical Ocean Prediction System (TOPS; Clancy and Martin 1981; Clancy and Pollack 1983) and is based on the level-2 turbulence closure of Mellor and Yamada (1974). The vertical mixing terms are expressed as

$$D_u = \overline{w'u'} = -lS_m q\frac{\partial u}{\partial z} = -K_{om}\frac{\partial u}{\partial z} \tag{45}$$

$$D_v = \overline{w'v'} = -lS_m q\frac{\partial v}{\partial z} = -K_{om}\frac{\partial v}{\partial z} \tag{46}$$

$$D_T = \overline{w'T'} = -lS_m q\frac{\partial T}{\partial z} = -K_{om}\frac{\partial T}{\partial z} \tag{47}$$

$$D_S = \overline{w'S'} = -lS_m q\frac{\partial S}{\partial z} = -K_{om}\frac{\partial S}{\partial z}, \tag{48}$$

where l is the mixing length, S_h and S_m are constants computed as functions of the Richardson number, K_{oh} and K_{om} are the ocean eddy mixing coefficients, and

$$q = (2e)^{1/2}, \tag{49}$$

where e is the turbulent kinetic energy. The details for the calculations of S_h and S_m are presented in Mellor and Yamada (1974). The turbulent kinetic energy is computed assuming a balance between the shear production, the buoyancy production, and the viscous dissipation,

$$lqS_m\left[\left(\frac{\partial u}{\partial z}\right)^2 + \left(\frac{\partial v}{\partial z}\right)^2\right] - lqS_h\left(\frac{g}{\rho}\frac{\partial \rho}{\partial z}\right) - \frac{q^3}{15l} = 0. \tag{50}$$

The mixing length l is expressed as

$$l = \frac{kz}{1 + (kz/l_0)}, \tag{51}$$

where k is the von Kármán constant (0.4) and l_0 is computed as

$$l_0 = \frac{0.1\displaystyle\int_{-H}^{0} |z| q\, dz}{\displaystyle\int_{-H}^{0} q\, dz}, \tag{52}$$

where H is the depth of the ocean.

The l_0 from the previous time step is used when solving (51). Optionally, an iteration could be performed each time step in the calculations of q and l, but experiments have shown that the solutions are not sensitive to this. Also, the mixing terms (45)–(48) are computed as adjustments at the end of each time step in an implicit formulation so that we are not constrained by the stability restrictions on K_{oh} and K_{om} necessary when using an explicit formulation of these terms. The horizontal

mixing in the ocean model consists only of a background fourth-order diffusion, similar to that used in the atmospheric model described above.

The lateral boundary conditions in the ocean model are similar to those used in the atmospheric model. Fixed-, periodic-, or radiation-type boundary conditions can be used. When using the radiative boundary conditions, all boundary values are set to their initial values for inflow points. At outflow points, (32) is used to predict the normal velocity component, while all other variables are linearly extrapolated to the boundary. The value of c_* is fixed at 10 m s^{-1}.

The upper boundary conditions on the vertical mixing terms are

$$-(\overline{u'w'}) = \left(\frac{\rho_a}{\rho_o}\right)u_*^2\frac{u}{|V|} \tag{53}$$

$$-(\overline{v'w'}) = \left(\frac{\rho_a}{\rho_o}\right)u_*^2\frac{v}{|V|} \tag{54}$$

$$-(\overline{w'T'}) = \left(\frac{\rho_a}{\rho_o}\right) - \left(u_*T_* + \frac{L_v u_* q_*}{C_p}\right) \tag{55}$$

$$-(\overline{w'S'}) = \left(\frac{\rho_a}{\rho_o}\right)(u_* q_* S - P), \tag{56}$$

where u_*, T_*, and q_{v*} are the scale values of velocity, temperature, and water vapor computed following Louis et al. (1982); ρ_a and ρ_o are the densities at the air–ocean interface of the atmosphere and ocean, respectively; and P is the precipitation. At the lower boundary, the normal gradient of the vertical mixing terms is assumed to vanish to prevent unrealistic tendencies from developing there.

e. Model coupling

COAMPS can be used as a stand-alone atmosphere or ocean forecast model or in an integrated fashion where both models exchange information across the air–ocean boundary. This exchange occurs at each ocean time step since typically the ocean time step is much larger than the atmospheric time step. The fluxes of heat, moisture, and momentum are averaged over all atmospheric time steps during one ocean time step. These average fluxes are then used as the upper boundary condition in the ocean model. Also, the total precipitation is summed over all atmospheric time steps during one ocean time step. This total precipitation is then incorporated into the ocean model as a source of freshwater. The temperature of the upper level of the ocean model is fixed as the SST during all atmospheric time steps within any one ocean time step.

3. Model results

Two examples of COAMPS prediction ability are presented. The first example is the application of the system to real-time support for the 1995 America's Cup sailboat races. In this example, it is demonstrated that COAMPS is a viable system for predicting mesoscale weather events that are forced primarily through interactions of large-scale flow with detailed surface features. In the second example, idealized simulations of a tropical cyclone are shown to illustrate COAMPS ability to predict mesoscale features found within these systems. Although this type of idealized simulation cannot be verified with real data, it can be used to show the extent to which COAMPS can simulate mesoscale features observed in the atmosphere with the hope that given the proper observations and assimilation techniques, real-time forecasts of features such as these could be possible in the future. The tropical cyclone simulations also contain an example of a forecast using both the atmosphere and ocean models in COAMPS. This simulation establishes the validity of the coupled system and shows the potential of coupled forecasts for the future.

a. Operational application of COAMPS to America's Cup

The COAMPS atmospheric model was tested in a real-time operational mode during March and April 1995 in support of the America^3 team in the 1995 America's Cup races. The forecasts were used to determine the type of near-surface wind conditions that would be present that day during the race to help the crew determine the most proper sails to use, boat configuration, and crew assignments. The COAMPS forecast was used as one forecast aid in the final determination of the local weather conditions expected during the race.

The logistics for each race day are as follows. The 1200 UTC (0400 PST) observational data and the NOGAPS analysis and 12- and 24-h forecast fields from the previous analysis time at 0000 UTC (1600 PST the previous day) were transferred via ftp from FNMOC to the San Diego Supercomputer Center (SDSC). Once this was complete, the COAMPS forecast was initiated on the SDSC Cray C90. Upon completion of the forecast, the appropriate COAMPS forecast information was sent to the America^3 compound for integration into their final forecast for the day. The transferring of the data, the execution of the COAMPS forecast, and the dissemination of the COAMPS forecast to the America^3 compound was performed by KTAADN personnel from Newton, Massachusetts.

A triply nested version of COAMPS was used with resolutions of 45, 15, and 5 km for the coarse, medium, and fine grids, respectively, and the Therry and Lacarrère (1983) subgrid-scale mixing option was used. The domain for each of the grids is shown in Fig. 1. The 30 vertical sigma levels were set at 10, 30, 55, 90, 140, 215, 330, 500, 750, 1100, 1600, 2300, 3100, 3900, 4800, 5800, 6800, 7800, 8675, 9425, 10 175, 10 925, 11 675, 12 425, 13 300, 14 300, 16 050, 19 400, 24 400, and 31 050 m. COAMPS produced 12-h forecasts using the

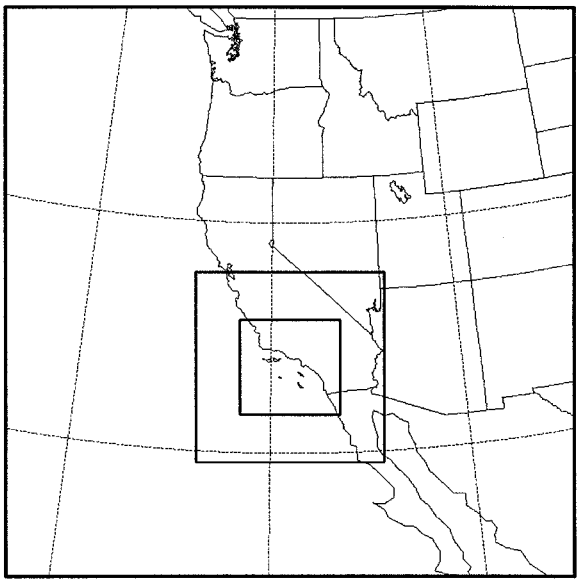

FIG. 1. Areal coverage of COAMPS domains for coarse-, medium-, and fine-mesh grids.

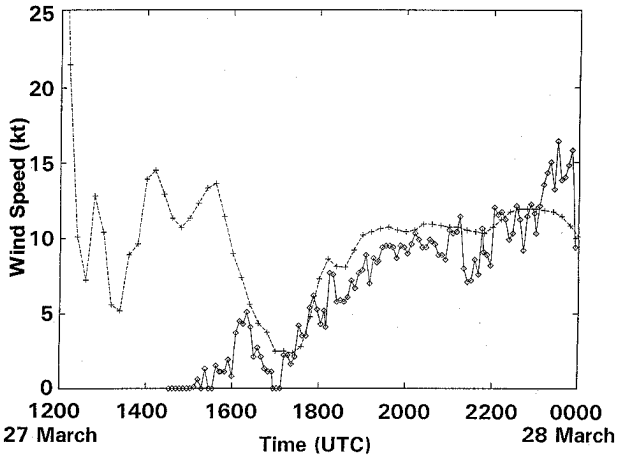

FIG. 2. Wind speed observations from the America³ boat (diamonds) and COAMPS forecast wind speeds (plus signs) for the point nearest the America³ boat from 1200 UTC 27 March 1995 to 0000 UTC 28 March 1995. Figure courtesy of Steve King, KTAADN.

0000 UTC NOGAPS 12-h forecasts for first-guess fields to the analysis, referred to here as a ''cold-start.'' This method led to two problems found in many of the forecasts. First, the only NOGAPS fields available were on the standard pressure levels, with the lowest level being 1000 mb. Typically this was at least 100 m above the surface, particularly over the water. For the initial fields, COAMPS simply interpolated the 1000-mb winds to all lower levels, often resulting in 10-m winds over the ocean that were much stronger than observed. Second, the use of the NOGAPS fields for the first guess led to large adjustments during approximately the first 4–6 h of most forecasts. This was caused by the adjustment of the coarser, global initial data (1° grid resolution) to the COAMPS higher-resolution grid, particularly in relation to the COAMPS topography and land–sea boundary. This adjustment is referred to here as the model spinup. During the first 4–6 h of each forecast, it was difficult to determine real changes from spurious changes associated with the model spinup. Results of one of the forecasts that exhibited both of these problems is shown in Fig. 2. This figure shows the time history of the 10-m wind speed near the race area taken onboard an America³ support boat compared to a COAMPS gridpoint forecast valid at 10 m over the surface nearest the support boat. The COAMPS initial 10-m wind speed is over 25 kt, stronger than any reports in the area at this time (not shown). During the first 4 h of the forecast (1200–1600 UTC), the forecast wind speed varied from 5 to 15 kt. At approximately 5 h into the forecast (1700 UTC), the wind speed was down to about 2 kt, and from this point on, the COAMPS forecast wind speed agreed favorably with the observed wind speed taken from an America³ support boat.

To correct these problems, the setup for the COAMPS forecasts was changed beginning in mid-April. Starting at this time, two COAMPS forecasts were made each race day. The first was a 12-h forecast from 0000 UTC (1600 PST the previous day) to 1200 UTC (0400 PST) on the day of the race using NOGAPS analyzed fields for the initial conditions as was done before, only now starting 12 h earlier. The 12-h COAMPS forecasts obtained from this run were then used for the first-guess fields for the subsequent 12-h forecast from 1200 UTC (0400 PST) to 0000 UTC (1600 PST) on the day of the race. The utilization of the previous COAMPS forecast as the first guess in the second run minimized the effect of the model spinup. As a result, more meaningful forecasts with better time continuity were made in spite of the fact that the COAMPS resolution was cut to 81, 27, and 9 km for the three meshes during the finals. The domain sizes were kept as close as possible to those shown in Fig. 1. The resolution was changed to allow for time to run the two 12-h forecasts instead of just one, as was done in March. The forecast for one specific America³ race utilizing the 12-h data assimilation is discussed next.

Coastal surface wind observations and the COAMPS 10-m wind forecasts valid at 2100 UTC (1300 PST) 26 April 1995 for portions of the coarse (81 km), medium (27 km), and fine mesh (9 km) grids are shown in Fig. 3. The observations indicate light (1–7 kt) south and southwesterly flow along the immediate coast near Los Angeles and San Diego, with a predominantly northwesterly flow (>8 kt) over the outer waters and along the coast to the north. This indicates the presence of a narrow trough just off the coast of southern California. In both the coarse and medium meshes, westerly winds are forecast along the California coast. However, in the fine mesh, a trough is present just off the coast, resulting in a south to southwesterly wind correctly forecast in

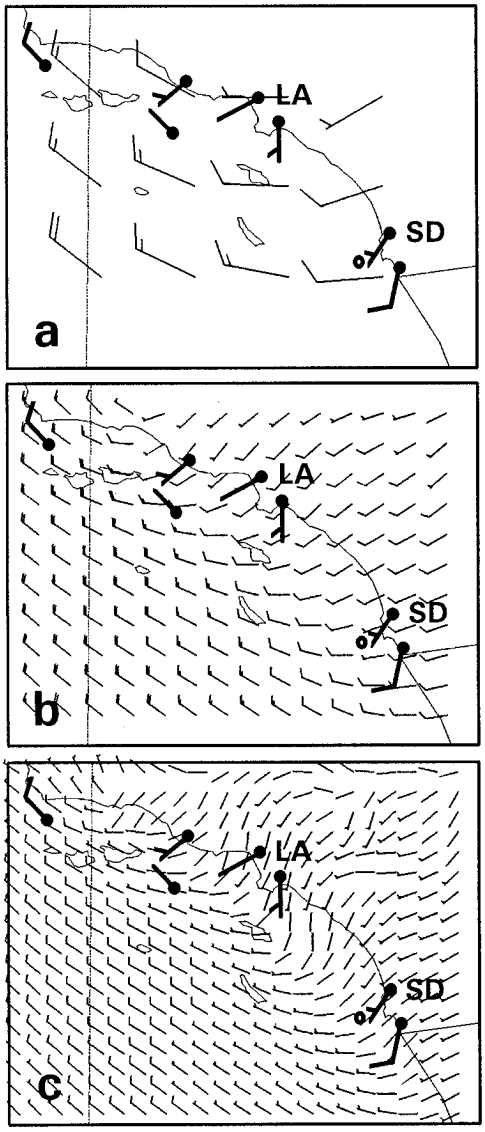

FIG. 3. COAMPS 9-h forecast 10-m wind field (light wind barbs) valid 2100 UTC 26 April 1995 over the same subgrid of the (a) coarse mesh, (b) medium mesh, and (c) fine mesh. Wind barbs are shown at each model point in (a) and (b) but are thinned to every other point in (c). Coastal surface wind observations valid at 2100 UTC 26 April 1995 are in bold. No barb indicates wind speed of 1–2 m s^{-1}, half-barb 3–7 m s^{-1}, and full barb 8–12 m s^{-1}. Open circle represents race location; LA indicates location of Los Angeles and SD indicates location of San Diego.

the vicinity of the race area. The speeds as represented in the fine mesh are forecast to be quite light (2–7 kt) in the race area, approximately one-half of the speed that was forecast in the coarser meshes and in agreement with the observations. A validation of the COAMPS fine-mesh wind speed forecast against the observed wind speeds from the America[3] support boat is shown in Fig. 4. This figure illustrates the improvements over the previous forecasts using a cold start. First, the initial COAMPS wind speed is about 2–3 kt, consistent with

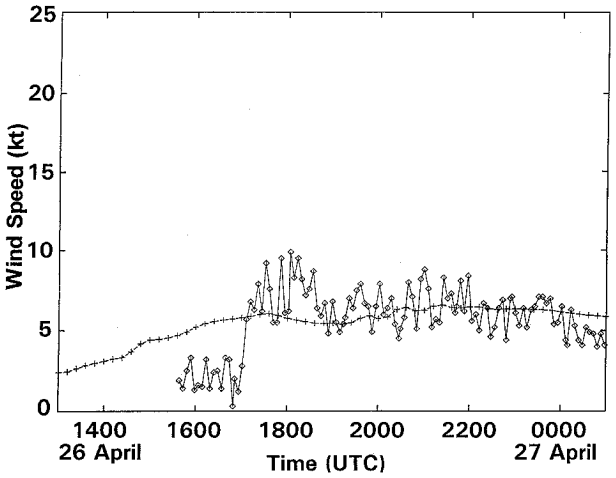

FIG. 4. As in Fig. 2 except from 1300 UTC 26 April 1995 to 0000 UTC 27 April 1995.

the light winds that prevailed over this area for several days preceding this forecast (not shown). Second, the time history of the wind speed, particularly during the first few hours, does not show the spurious signal attributed to model spinup in previous forecasts. The observations indicate wind speeds generally from 4 to 8 kt, while the COAMPS forecast indicates wind speeds of 5–6 kt. This is an improvement over the coarse and medium meshes, which forecast wind speeds in the vicinity of 8–12 kt. Presumably, the improved wind forecasts in the fine mesh are due to the better definition of the terrain and coastline in this mesh.

This forecast demonstrates the improvements that can be obtained through the use of nested grids to attain high resolution in areas of strong surface forcing. Although the initial fields were provided from a relatively coarse analysis, the high-resolution model was able to quickly and accurately adjust the flow due to the complex terrain in the forecast domain. Also, the introduction of data assimilation, that is, using a COAMPS forecast for the first guess, resulted in 6–12-h forecasts that displayed considerably more consistency and integrity than those produced from a cold-start. This is significant if mesoscale models such as the ones contained in COAMPS are to be used in analysis, nowcast, and short-term forecast (0–24 h) systems. The model spinup in cold-start runs can render the forecasts useless for predicting trends, particularly during the early stages of the forecast. The use of data assimilation by the mesoscale system allows not only the introduction of current observations into the system but also the carrying of history of the previous data, as represented by the mesoscale model, forward in time as well.

b. Idealized tropical cyclone simulations

Two 84-h tropical cyclone simulations using COAMPS are presented to demonstrate the ability to

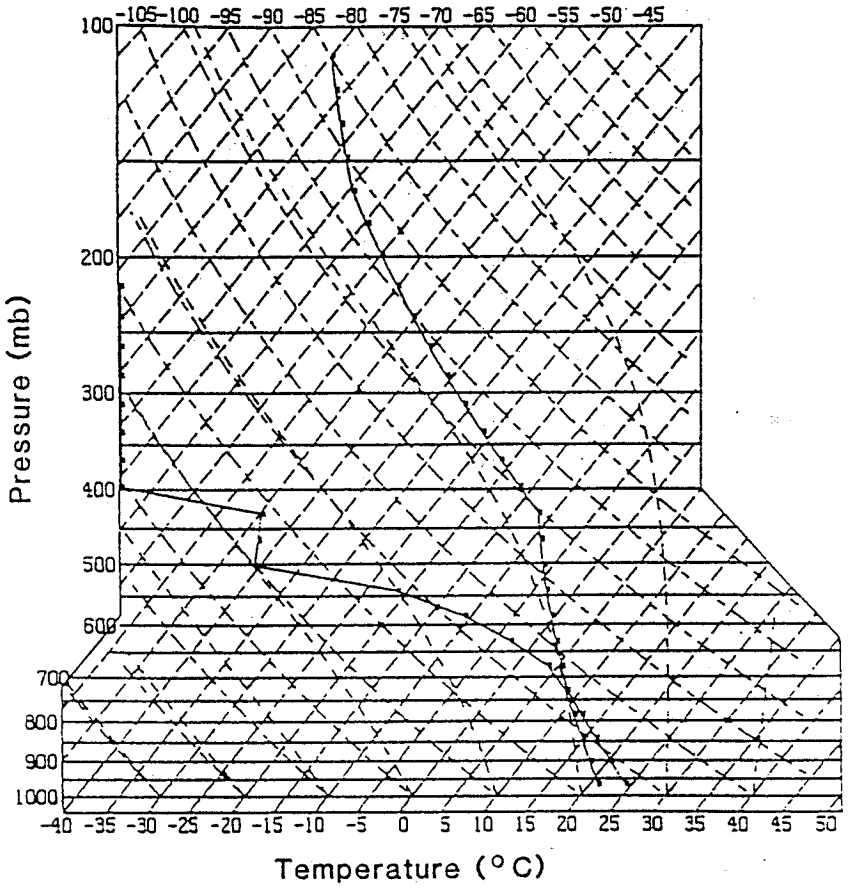

FIG. 5. Skew T–log$p$ diagram with Kingston, Jamaica, sounding for 0000 UTC 11 September 1988.

model the tropical cyclone as well as the accompanying air–ocean coupling. In the first simulation (SIM1), only the COAMPS atmospheric model is used and the SST is fixed in time. In the second simulation (SIM2), the fully coupled COAMPS system is used. Here the SST is taken as the temperature of the uppermost level in the COAMPS ocean model, which changes in time due to induced ocean circulations, mixing processes, and the sensible heat flux. The initial data for these simulations are representative of the conditions observed in the vicinity of Hurricane Gilbert, which moved through the Caribbean Sea and the Gulf of Mexico during September 1989. This does not mean that SIM1 and SIM2 are simulations of Gilbert, but rather they represent simulations of systems that could develop given the general environmental conditions observed at a position close to Gilbert in both space and time.

The initial atmospheric conditions are the same for both SIM1 and SIM2. The temperature and moisture profiles taken at Kingston, Jamaica, valid at 0000 UTC 11 September 1989 (Fig. 5) are used. In addition, the relative humidity is arbitrarily set to 0.05% from 5500 to 7100 m and to 0.005% above 7100 m. A Rankine vortex, positioned at the center of the grid, is used to specify the initial wind field. Inside the radius of maximum winds $r_{\max}$, the tangential velocity v_θ is computed as

$$v_\theta = v_{\max}\left(\frac{r}{r_{\max}}\right), \tag{57}$$

where $v_{\max}$ is the maximum tangential velocity (15 m s^{-1}), r is the distance from the center of the storm, and $r_{\max}$ is set to 90 km. Outside $r_{\max}$,

$$v_\theta = v_{\max}\left(\frac{r}{r_{\max}}\right)^x\left(1 - \frac{r^2}{r_{\text{in}}^2}\right), \tag{58}$$

where $x = 0.6$ is an empirical constant and r_{in} is the radius of influence (240 km), beyond which v_θ is set to zero. This wind pattern is used from the surface to 10 km. The wind exponentially decreases to zero from 10 to 13 km and is set to zero above 13 km. Since no mean flow was used and the simulations were performed on an f plane (17.5°N), the tropical cyclone remains fixed in the center of the grid for the the full length of the simulations. The initial pressure field is computed using the balance equation obtained from the horizontal equations of motion, assuming the time tendency of the di-

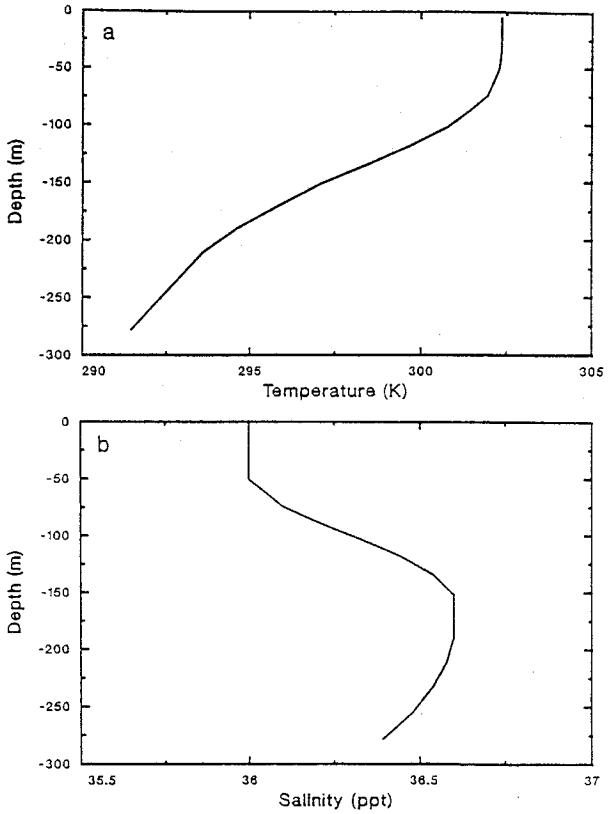

FIG. 6. (a) Initial ocean temperature (K) profile for SIM2. (b) As in (a) except for salinity.

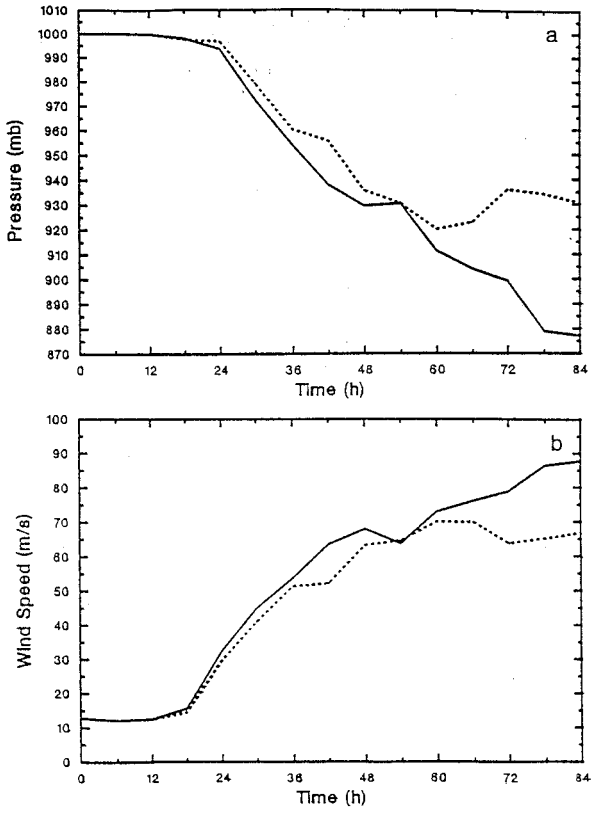

FIG. 7. (a) COAMPS forecast central pressure (mb) for SIM1 (solid) and SIM2 (dashed) from 0 to 84 h. Values are plotted in 6-h increments. (b) As in (a) except for maximum wind speed.

vergence is zero. The perturbation potential temperature is computed hydrostatically from the initial pressure field.

The initial ocean data for SIM1 and SIM2 is obtained from the Generalized Digital Environmental Model (GDEM; Teague et al. 1990) for the month of September at a position near where Gilbert attained maximum intensity (19.8°N, 83.9°W). The GDEM profiles of temperature and salinity, used to initialize all COAMPS ocean model points, are shown in Fig. 6. In SIM1, the GDEM temperature at 2.5 m is used as the SST. In SIM2, the temperature and salinity values in Fig. 6 are interpolated to the model levels. Since the top ocean model level is 5 m deep, the initial SST in SIM1 and SIM2 are exactly the same.

The grid used in the atmospheric model for SIM1 and SIM2 is as follows. A Cartesian grid consisting of 61 points in the east–west and north–south directions with a horizontal grid spacing of 10 km is used. The model uses 30 vertical levels with a constant vertical spacing of 600 m. Radiative boundary conditions are used on the lateral boundaries. The ocean model also uses a 61 $\times$ 61 Cartesian grid so that the grid points for the atmosphere and ocean are coincident. In SIM2, the ocean model uses 20 vertical layers, with the spacing set at 5 m for the uppermost layer and each successively lower layer 1 m more in depth. Therefore, the total depth of the ocean is 290 m.

The coupling between the atmosphere and ocean in SIM2 is performed as follows. Since the large time step of the atmospheric model is 30 s and the large time step of the ocean model is 1200 s, all exchanges to the ocean occurred every large ocean time step. This is accomplished by integrating the atmospheric model first for 40 time steps (i.e., one large ocean time step) using a constant SST, with the SST being defined as the temperature of the uppermost model layer. The surface fluxes of heat, moisture, and momentum are averaged and the precipitation reaching the earth's surface is accumulated during these 40 atmospheric time steps. These average fluxes and total precipitation are then used as upper boundary conditions for the ocean subgrid-scale mixing processes. The new SST is then used for the next 40 atmospheric time steps, and the time-stepping process is repeated for the length of the forecast.

The COAMPS forecast central pressure and maximum wind speed for SIM1 and SIM2 are shown in Fig. 7. Two distinct stages of development are present in SIM1. In the first stage, defined as the first 24 h of the simulation, the central pressure remains nearly constant at 1000 mb. During this stage, the model storm develops a low-level inflow in response to the surface friction

and a warm, moist PBL due to the sensible and latent heat fluxes. This leads to an initial spindown of the storm circulation for approximately the first 12 h until the induced upward motion initiates convection. This convection forms near the radius of maximum winds, initially set at 90 km, but rapidly contracts inward. The maximum wind speed starts increasing at 19 h of the simulation, during which time the minimum pressure remains constant. The increase of the maximum wind prior to the central pressure fall is similar to that reported by Rosenthal (1978). The increase in wind speed occurs about 12 h after the first convective towers formed in the eyewall. However, it is only 2 h after the development of ice crystals atop the eyewall convection. This suggests that the added heat release due to the formation of the ice clouds may be a significant factor in causing the deepening of the system as found by Tripoli (1992b). In the second stage, defined as the last 60-h period from 24 to 84 h of the simulation, the model storm exhibits rapid deepening, with the central pressure falling from 1000 to 874 mb.

The central pressure in SIM1 rose and then fell dramatically between 48 and 60 h, which coincides with the formation of spiral bands of convection. These bands acted as a dynamic part of the system, occasionally contracting inward toward the eye with noticeable changes on the central pressure and maximum wind speed. Willoughby et al. (1982) noted that concentric eyewalls have been observed in intense, symmetric hurricanes. Furthermore, they reported that the outermost concentric ring of convection typically contracts inward, thereby weakening the innermost ring of convection until the outer ring replaces the inner ring as the eyewall. During the period of the contraction of the outer ring, the storms were observed to weaken in intensity, with rapid intensification following the replacement of the eyewall by the outer ring. Other observational studies (Fortner 1958; Jordan and Schatzle 1961; Jordan 1966; Holliday 1977; Willoughby et al. 1982) show that the eye of the storm is somewhat larger after the replacement of the inner eyewall by the outer eyewall. Shapiro and Willoughby (1982) demonstrated that a heat source, such as from convection, near a maximum in tangential wind leads to larger height falls inside the radius of maximum winds than outside. This leads to a propagation inward of the tangential wind maximum and the associated heat source. The contraction of the wind maximum often leads to a destruction of an inner wind maximum and an eventual replacement by the outer wind maximum.

One of the most significant occurrences of concentric eyewall collapse is found in SIM1 during the period from 48 to 60 h. Model-generated radar reflectivities at 3300 m at 48, 50, 52, 54, 56, and 57 h are given in Fig. 8. At 48 h, a ring of convection is found around the eye with the newly formed spiral bands over 100 km from the center of the storm. The maximum reflectivity in the eyewall is found 20–30 km from the eye. Over the next 6 h, the spiral bands slowly converge in toward the eye, forming a nearly closed ring of convection around the eye at a radius of about 70 km by 54 h. By this time, the radar reflectivities are larger in the outer eyewall than in the inner eyewall. At 56 h, it appears that the outer and inner eyewalls are merging into one. Individual cloud elements make up a relatively disorderly pattern of convection from 20 to 60 km from the eye. One hour later, at 57 h, the concentric rings have merged into one eyewall, with the maximum reflectivities now about 35–40 km from the eye.

The central pressure and maximum wind speeds for the time period of 48–60 h are shown in Fig. 9 with a higher temporal resolution than was used in Fig. 7. From 48 to 50.5 h, the period in which the spiral band was still at least 80 km from the eye, the pressure continued to fall and the wind speed continued to rise. From 50.5 to 54.25 h, the time period over which the outer eyewall contracted from 80 to 60 km, the central pressure rose 6.5 mb and the maximum wind decreased 8.5 m s^{-1}. Only after 54.25 h, when the outer and inner eyewalls began to merge, did the central pressure begin to fall again with a corresponding increase in the maximum winds. Rapid intensification occurred during the one hour time period from 57 to 58 h with the central pressure falling 9.6 mb from 924.3 to 914.7 mb and the maximum winds increasing from 69.3 to 74.0 m s^{-1}. This intensification was short lived, however, when the spiral bands started contracting inward toward the eye again by 60 h. As noted above, the radius of the eye increased from about 25 to 40 km during the merging of the two concentric eyewalls.

Three stages of development are noted in SIM2. The first stage is the same as that described earlier for SIM1. In the second stage of SIM2, defined as the 36-h period from 24 to 60 h of the simulation, the model storm deepens rapidly with the central pressure falling from 1000 to 920 mb, very similar to what occurred in SIM1. However, during the third stage of SIM2, defined as the last 24-h period from 60 to 84 h of the simulation, the model storm achieves a quasi-steady state with the central pressure varying from 920 to 940 mb. During the period from 24 to 60 h, the central pressure in SIM2 is 5–10 mb higher and the maximum wind speed is 2–10 m s^{-1} less than in SIM1. However, by 84 h, SIM2 is significantly weaker than SIM1, with the SIM2 central pressure 53.5 mb higher and the maximum wind speed 21 m s^{-1} less than in SIM1.

The growing differences between SIM1 and SIM2 throughout the simulations is due to the change in the SST in SIM2. The SST in SIM2 at 10-km radius from the center of the storm is shown in Fig. 10. During the first 42 h, the SST exhibited cooling of less than 0.5°C due to the relatively light winds present during this time period. After 42 h, the cooling increased dramatically, with SST changes of −5.7°C by 60 h, and −8°C at 84 h. At radii beyond about 50 km, the SST cooling was less than 0.5°C. From these SST changes, it is understandable that there are relatively small differences be-

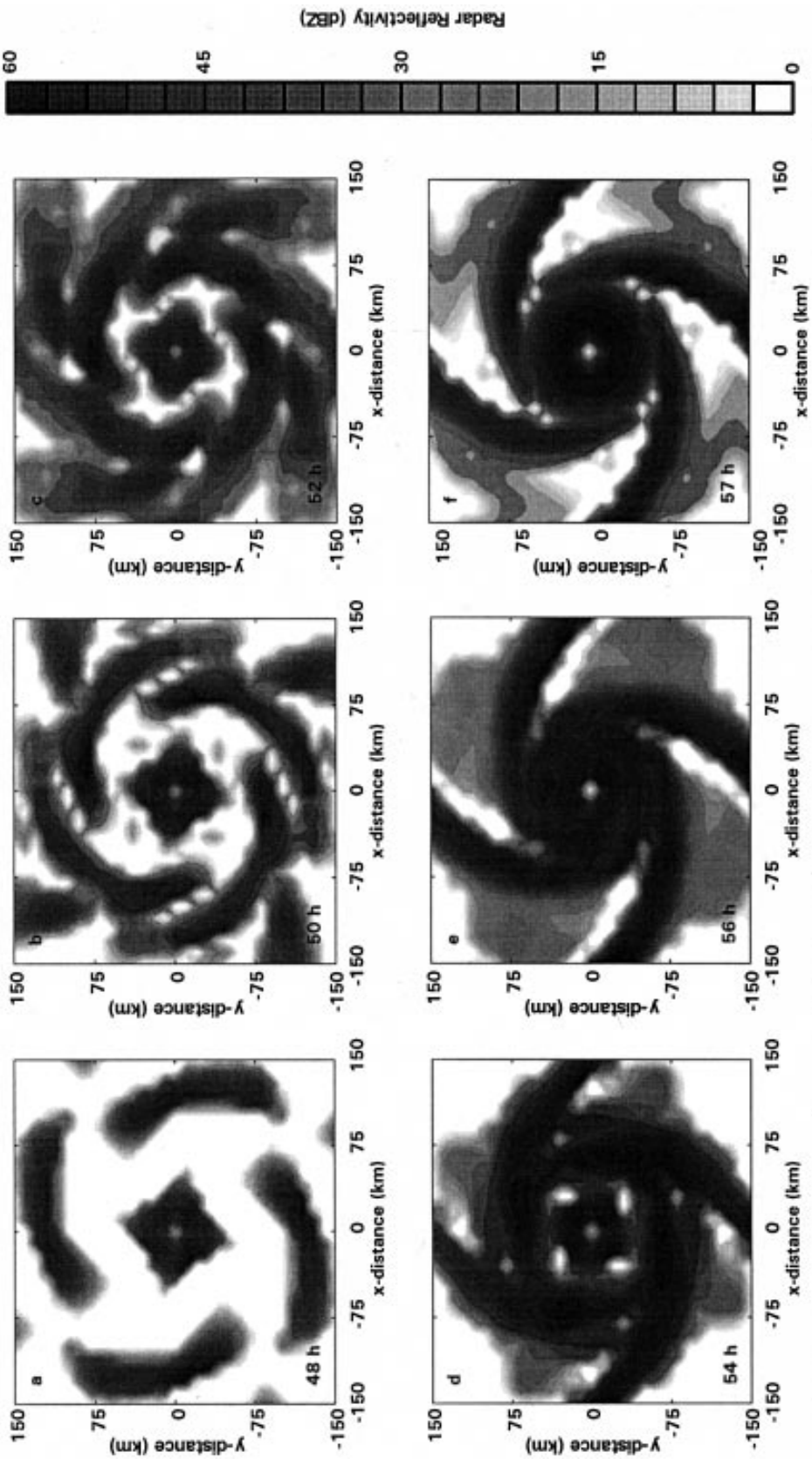

FIG. 8. Model-generated radar reflectivities at 3300 m for SIM1 over central 21 × 21 grid points at (a) 48, (b) 50, (c) 52, (d) 54, (e) 56, and (f) 57 h.

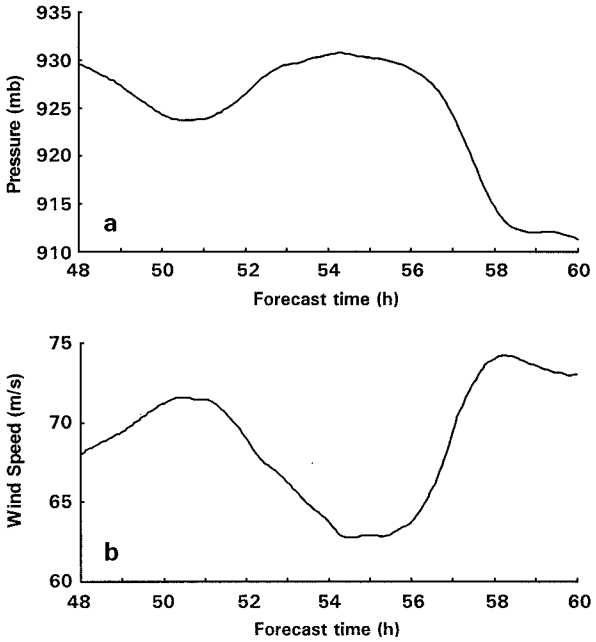

FIG. 9. (a) Minimum central pressure (mb) forecast for SIM1 from 48 to 60 h. Values plotted every time step (30 s). (b) As in (a) except for maximum wind speed.

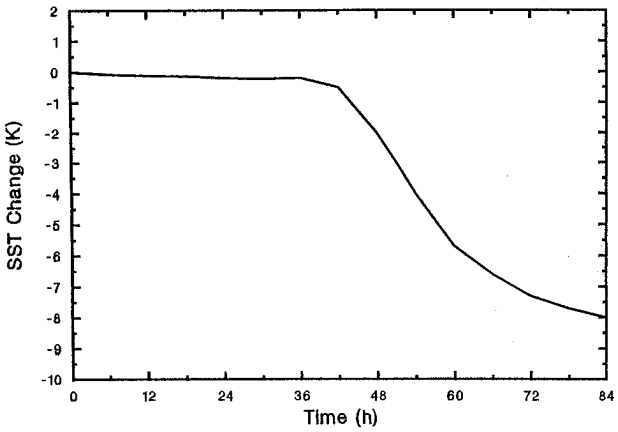

FIG. 10. SST (K) at 10 km from center of tropical cyclone in SIM2 for 0 to 84 h.

tween the strength of the tropical cyclone in SIM1 and SIM2 during the first 42 h. However, since the SST dropped over 5°C from 42 to 60 h with no significant weakening occurring in the strength of the tropical cyclone in SIM2 until after 60 h, it appears that there is a time lag on the order of 12 h between strong surface cooling near the eyewall and corresponding changes in the storm intensity. This result is similar to that found by Chang and Anthes (1979).

The SST changes of 8°C reported here are somewhat larger than the 5°–6°C reduction actually observed for Hurricane Gilbert (Shay et al. 1991). This can partially be explained by the fact that in SIM2, the model storm remained stationary for all 84 h of the simulation, and therefore all the mixing and upwelling responsible for the SST reduction remained concentrated over the same area. In reality, Gilbert moved westward to west-northwestward at a speed of about 7 m s^{-1} and the SST cooling processes were isolated over a given area for a much shorter period of time. These findings indicate that SST cooling may have little effect on tropical cyclone strength for storms with a movement of as little as 1–2 m s^{-1}. Since the storm is moving, it will continuously be entering areas of undisturbed SST, unless of course, the storm loops back over an area recently disturbed by perhaps another tropical cyclone. Also, since there appears to be a time lag of perhaps 12 h between that strong SST cooling and a response to the hurricane strength, a forward speed of 1–2 m s^{-1} will enable the eyewall region of the storm to move away from the cooler SST before it can have a significant impact on the eyewall.

The differences in the SIM1 and SIM2 tangential velocities at 48 and 84 h can be seen in Fig. 11. At 48 h, both SIM1 and SIM2 exhibit maximum tangential velocities of 62 m s^{-1} at a radius of 20 km. The tangential wind profiles are nearly constant with height up to 5 km, with the winds decreasing above this level. By 84 h, the most significant differences are found in the eyewall region. Besides SIM2 exhibiting a maximum tangential velocity of 67 m s^{-1} as opposed to 85 m s^{-1} in SIM1, the radius of the maximum wind in SIM2 is 10 km larger than in SIM1. Also, the gradient of the tangential velocity from the maximum to the eye is significantly weaker in SIM2. At radii beyond about 50 km, only small differences exist in the tangential velocity profiles. This indicates that while the intensities (based on the maximum wind speed) of the SIM1 and SIM2 storms are different, their strengths (based on winds outside the radius of maximum winds) appear to be quite similar. This suggests that modification of the SST by a tropical cyclone may have little or no effect on the subsequent short-term (0–36 h) track of the storm due to any forced changes in structure since the SST changes will only affect the intensity and not the overall strength of the storm (Holland 1984; DeMaria 1985).

These tropical cyclone simulations demonstrate two points. The first is that mesoscale models are capable of making realistic simulations of mesoscale features such as convective eyewalls. The second is that it is possible to construct a coupled ocean–atmosphere system for prediction of events where this coupling has a significant impact on the development of both the atmospheric and oceanic structures. This indicates that it may be possible to predict, on a real-time basis, mesoscale events that are not necessarily forced by surface irregularities if we can routinely measure these systems and assimilate this data into the model initial conditions.

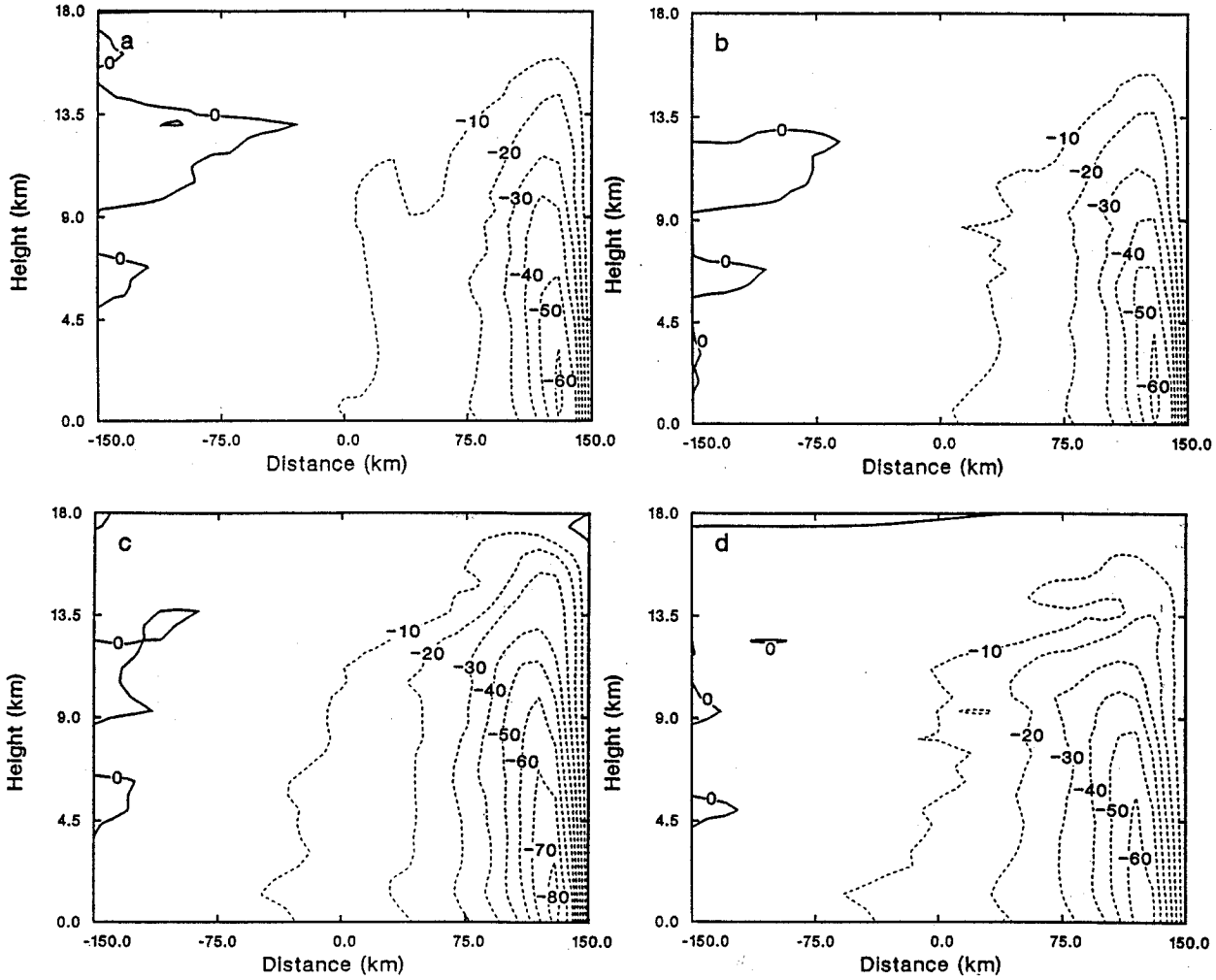

FIG. 11. East–west vertical cross sections of tangential velocity (m s^{-1}) taken from the left boundary to the center of the grid shown in Fig. 2 for (a) SIM1 at 48 h, (b) SIM2 at 48 h, (c) SIM1 at 84 h, and (d) SIM2 at 84 h.

4. Summary and future plans

The three-dimensional Coupled Ocean/Atmosphere Mesoscale Prediction System (COAMPS) has been developed by NRL. COAMPS is composed of a multinested nonhydrostatic atmospheric model and a hydrostatic ocean model. The atmospheric model contains parameterizations for subgrid-scale mixing, cumulus parameterization, radiation, and explicit moist physics, while the ocean model includes a parameterization for subgrid-scale mixing. The models can be integrated simultaneously so that precipitation and the surface fluxes of heat, moisture, and momentum are exchanged across the air–ocean interface every time step. Optionally, either model can be used as a stand-alone system. The atmospheric model can be used for operational mesoscale forecasting using observational data or idealized experiments.

Two applications of COAMPS have been presented here. The first application involved the use of the atmospheric model for real-time support of the America^3 team in the 1995 America's Cup races. In this application, COAMPS, using a resolution of 9 km, provided 12-h forecasts for days on which America^3 sailed. It was found that a 12-h data assimilation cycle was necessary to reduce the effects of model spinup that resulted from initializing COAMPS with global fields. This represents the current state of the art in operational mesoscale modeling: the ability to predict mesoscale features that are generated from the interaction of synoptic-scale flow with surface irregularities.

In the second application, two simulations of a tropical cyclone were discussed; one using only the COAMPS atmospheric model with a fixed SST, while the second used both the atmospheric and ocean models of COAMPS in a fully coupled mode. In the uncoupled simulation, COAMPS successfully developed a realistic eyewall and was able to simulate the inward propagation of concentric eyewalls as has been observed in numer-

ous tropical cyclones. In the coupled simulation, it was found that the tropical cyclone induced strong SST cooling within the radius of maximum winds, resulting in a weakening of the tropical cyclone. The time and spatial scales of the SST cooling suggest that the SST changes would probably have a relatively small effect on the future short-term (0–36 h) storm strength and track, providing the tropical cyclone maintains a movement of at least 1 m s^{-1}. Increased observations and advanced assimilation methods are needed to predict these types of features on a routine basis. This represents the future challenge for operational mesoscale modeling: to assimilate mesoscale observations for the purpose of providing consistent and accurate analyses and forecasts of mesoscale features that are not necessarily forced by interaction of synoptic-scale flow with surface irregularities.

Further improvements to COAMPS are being developed. For the atmospheric model, these include improvements to the surface parameters database to reflect the latest high-resolution fields, adjoint development for sensitivity studies and use in an improved data assimilation scheme, digital filter initialization, moisture analysis, and the ability to use the model for large-eddy simulations. Improvements to the ocean model include the introduction of terrain, data assimilation for real data simulations, and improved lateral boundary conditions.

Acknowledgments. The author wishes to express his gratitude to Dr. John Hovermale for originating the concept of COAMPS and for his encouragement and guidance in its development. Helpful contributions for COAMPS model development were provided by Simon Chang, James Doyle, Tracy Haack, Teddy Holt, Hung-Chi Kuo, Jerry Schmidt, and Liang Xu. Jack Kain provided the code for the Kain–Fritsch convective parameterization scheme, and Steve Rutledge provided the code for the explicit moist physics parameterization. Helpful discussions with Steve Burk, John Glendening, Jack Kain, Wendell Nuss, Melvyn Shapiro, and William Thompson also contributed to this work. The support of the sponsors, the Office of Naval Research through programs PE-0602435N and PE-0602704N and the Naval Research Laboratory through program ARI PE-0601153N, is gratefully acknowledged. This work was supported in part by a grant of HPC time from the Department of Defense Shared Resource Center, U.S. Army Corps of Engineers Waterways Experiment Station HPC Center, and performed on a Cray C-90. Additional computer resources were graciously provided by Fleet Numerical Meteorology and Oceanography Center (FNMOC) and the San Diego Supercomputer Center (SDSC).

REFERENCES

Baker, N. L., 1992: Quality control for the U.S. Navy operational database. *Wea. Forecasting,* **7,** 250–261.

Barker, E. H., 1980: Solving for temperature using unnaturally latticed hydrostatic equations. *Mon. Wea. Rev.,* **108,** 1260–1268.

Carpenter, K. M., 1979: An experimental forecast using a non-hydrostatic model. *Quart. J. Roy. Meteor. Soc.,* **105,** 629–655.

Chang, S. W., 1985: Deep ocean response to hurricanes as revealed by an ocean model with free surface. Part I: Axisymmetric case. *J. Phys. Oceanogr.,* **15,** 1847–1858.

——, and R. A. Anthes, 1979: The mutual response of the tropical cyclone and the ocean. *J. Phys. Oceanogr.,* **9,** 128–135.

Chorin, A. J., 1967: A numerical method for solving incompressible viscous flow problems. *J. Comput. Phys.,* **2,** 12–16.

Clancy, R. M., and P. J. Martin, 1981: Synoptic forecasting of the oceanic mixed layer using the navy's operational environmental database: Present capabilities and future applications. *Bull. Amer. Meteor. Soc.,* **62,** 770–784.

——, and K. D. Pollak, 1983: A real-time synoptic ocean thermal analysis/forecast system. *Progress in Oceanography,* Vol. 12, Pergamon Press, 383–424.

Clark, T. L., 1977: A small scale dynamic model using a terrain-following coordinate transformation. *J. Comput. Phys.,* **24,** 186–215.

——, 1979: Numerical simulations with a three-dimensional cloud model: Lateral boundary condition experiments and multicellular severe storm simulations. *J. Atmos. Sci.,* **36,** 2191–2215.

Davies, H. C., 1976: A lateral boundary formulation for multi-level prediction models. *Quart. J. Roy. Meteor. Soc.,* **102,** 405–418.

Deardorff, J. W., 1980: Stratocumulus-capped mixed layers derived from a three-dimensional model. *Bound.-Layer Meteor.,* **18,** 495–527.

DeMaria, M., 1985: Tropical cyclone motion in a nondivergent barotropic model. *Mon. Wea. Rev.,* **113,** 1199–1210.

Droegemeier, K. K., and R. B. Wilhelmson, 1987: Numerical simulation of thunderstorm outflow dynamics. Part I: Outflow sensitivity experiments and turbulence dynamics. *J. Atmos. Sci.,* **44,** 1180–1210.

Dudhia, J., 1993: Nonhydrostatic version of the Penn State–NCAR Mesoscale Model: Validation tests and simulation of an Atlantic cyclone and cold front. *Mon. Wea. Rev.,* **121,** 1493–1513.

Durran, D. R., and J. B. Klemp, 1983: A compressible model for the simulation of moist mountain waves. *Mon. Wea. Rev.,* **111,** 2341–2361.

Fortner, L. E., 1958: Typhoon Sarah, 1956. *Bull. Amer. Meteor. Soc.,* **39,** 633–639.

Gal-Chen, T., and R. C. J. Somerville, 1975: On the use of a coordinate transformation for the solution of the Navier–Stokes equations. *J. Comput. Phys.,* **17,** 209–228.

Gill, A. E., 1982: *Atmosphere–Ocean Dynamics.* Academic Press, 662 pp.

Harshvardhan, R. Davies, D. Randall, and T. Corsetti, 1987: A fast radiation parameterization for atmospheric circulation models. *J. Geophys. Res.,* **92,** 1009–1015.

Hogan, T. F., and T. E. Rosmond, 1991: The description of the U.S. Navy Operational Global Atmospheric Prediction System's spectral forecast model. *Mon. Wea. Rev.,* **119,** 1786–1815.

Holland, G. J., 1984: Tropical cyclone motion: A comparison of theory and observation. *J. Atmos. Sci.,* **41,** 68–75.

Holliday, C. R., 1977: Double intensification of Typhoon Gloria, 1974. *Mon. Wea. Rev.,* **105,** 523–528.

Jordan, C. L., 1966: The thermal structure of the core of tropical cyclones. *Geophysics,* **6,** 281–297.

——, and F. J. Schatzle, 1961: The ''double-eye'' of Hurricane Donna. *Mon. Wea. Rev.,* **89,** 354–356.

Kain, J. S., 1990: A one-dimensional entraining–detraining plume model and its application in convective parameterization. *J. Atmos. Sci.,* **47,** 2784–2802.

——, and J. M. Fritsch, 1993: Convective parameterization for mesoscale models: The Kain–Fritsch scheme. *The Representation of Cumulus Convection in Numerical Models, Meteor. Monogr.,* No. 46. Amer. Meteor. Soc., 165–170.

Klemp, J., and R. Wilhelmson, 1978: The simulation of three-di-

mensional convective storm dynamics. *J. Atmos. Sci.,* **35,** 1070–1096.

Lorenc, A. C., 1986: Analysis methods for numerical weather prediction. *Quart. J. Roy. Meteor. Soc.,* **112,** 1177–1194.

Louis, J. F., 1979: A parametric model of vertical eddy fluxes in the atmosphere. *Bound.-Layer Meteor.,* **17,** 187–202.

——, M. Tiedtke, and J. F. Geleyn, 1982: A short history of the operational PBL-parameterization at ECMWF. *Workshop on Planetary Boundary Parameterization,* Reading, United Kingdom, ECMWF, 59–79.

Mellor, G., and T. Yamada, 1974: A hierarchy of turbulence closure models for planetary boundary layers. *J. Atmos. Sci.,* **31,** 1791–1806.

Miller, M. J., and R. P. Pearce, 1974: A three-dimensional primitive equation model of cumulonimbus convection. *Quart. J. Roy. Meteor. Soc.,* **100,** 133–154.

——, and A. J. Thorpe, 1981: Radiation conditions for the lateral boundaries of limited-area numerical models. *Quart. J. Roy. Meteor. Soc.,* **107,** 615–628.

Ogura, Y., and J. Charney, 1962: A numerical model of thermal convection in the atmosphere. *Proc. Int. Symp. on N. W. P.,* Tokyo, Japan, Meteorological Society of Japan, 431–451.

——, and N. W. Phillips, 1962: Scale analysis of deep and shallow convection in the atmosphere. *J. Atmos. Sci.,* **19,** 173–179.

Perkey, D. J., and C. W. Krietzberg, 1976: A time-dependent lateral boundary scheme for limited-area primitive equation models. *Mon. Wea. Rev.,* **104,** 744–755.

Robert, A. J., 1966: The investigation of a low order spectral form of the primitive meteorological equations. *J. Meteor. Soc. Japan,* **44,** 237–245.

Rosenthal, S. L., 1978: Numerical simulation of a tropical cyclone development with latent heat release by the resolvable scales. I: Model description and preliminary results. *J. Atmos. Sci.,* **35,** 258–271.

Rutledge, S. A., and P. V. Hobbs, 1983: The mesoscale and microscale structure of organization of clouds and precipitation in midlatitude cyclones. VIII: A model for the ''seeder-feeder'' process in warm-frontal rainbands. *J. Atmos. Sci.,* **40,** 1185–1206.

Schlesinger, R. E., 1975: A three-dimensional numerical model of an isolated deep convective cloud: Preliminary results. *J. Atmos. Sci.,* **32,** 934–957.

Schumann, U., 1987: Influence of mesoscale orography on idealized cold fronts. *J. Atmos. Sci.,* **44,** 3423–3441.

Shapiro, L. J., and H. E. Willoughby, 1982: The response of balanced hurricanes to local sources of heat and momentum. *J. Atmos. Sci.,* **39,** 378–394.

Shay, L. K., P. G. Black, J. D. Hawkins, R. L. Elsberry, and A. J. Mariano, 1991: Sea surface temperature response to Hurricane Gilbert. Preprints, *19th Conf. on Hurricanes and Tropical Meteorology,* Miami, FL, Amer. Meteor. Soc., 574–578.

Skamarock, W. C., and J. B. Klemp, 1992: The stability of time-split numerical methods for the hydrostatic and the nonhydrostatic elastic equations. *Mon. Wea. Rev.,* **120,** 2109–2127.

Tapp, M. C., and P. W. White, 1976: A nonhydrostatic mesoscale model. *Quart. J. Roy. Meteor. Soc.,* **102,** 277–296.

Teague, W. J., M. J. Carron, and P. J. Hogan, 1990: A comparison between the generalized environmental model and Levitus climatologies. *J. Geophys. Res.,* **95,** 7167–7183.

Therry, G., and P. Lacarrère, 1983: Improving the kinetic energy model for planetary boundary layer description. *Bound.-Layer Meteor.,* **25,** 63–88.

Tripoli, G. J., 1992a: A nonhydrostatic mesoscale model designed to simulate scale interaction. *Mon. Wea. Rev.,* **120,** 1342–1359.

——, 1992b: An explicit three-dimensional nonhydrostatic numerical simulation of a tropical cyclone. *Meteor. Atmos. Phys.,* **49,** 229–254.

——, and W. R. Cotton, 1982: The Colorado State University three-dimensional cloud/mesoscale model—1982. Part I: General theoretical framework and sensitivity experiments. *J. Rech. Atmos.,* **16,** 185–220.

Willoughby, H. E., J. Clos, and M. Shoreibah, 1982: Concentric eyewalls, secondary wind maxima, and the evolution of the hurricane vortex. *J. Atmos. Sci.,* **39,** 395–411.

Xue, M., and A. J. Thorpe, 1991: A mesoscale model using the nonhydrostatic pressure-based sigma-coordinate equations: Model experiments with dry mountain flows. *Mon. Wea. Rev.,* **119,** 1168–1185.